1 Modelling the impact of clot fragmentation
2 on the microcirculation after thrombectomy

3   Wahbi K. El-Bouri[1,2*], Andrew MacGowan[1], Tamás I. Józsa[1], Matthew J. Gounis[3], Stephen J. Payne[1]

4   [1] Institute of Biomedical Engineering, Department of Engineering Science, University of Oxford,

5   Oxford, UK

6   [2] Liverpool Centre for Cardiovascular Science, Department of Cardiovascular and Metabolic Medicine,

7   University of Liverpool, Liverpool, UK

8   [3] New England Center for Stroke Research, Department of Radiology, University of Massachusetts

9   Medical School, Worcester, Massachusetts, USA

10   * Corresponding author

11   E-mail: w.el-bouri@liverpool.ac.uk (WKEB)

1   Abstract

13   Many ischaemic stroke patients who have a mechanical removal of their clot (thrombectomy) do not

14   get reperfusion of tissue despite the thrombus being removed. One hypothesis for this 'no-reperfusion'

15   phenomenon is micro-emboli fragmenting off the large clot during thrombectomy and occluding

16   smaller blood vessels downstream of the clot location. This is impossible to observe in-vivo and so we

17   here develop an in-silico model based on in-vitro experiments to model the effect of micro-emboli on

18   brain tissue. Through in-vitro experiments we obtain, under a variety of clot consistencies and

19   thrombectomy techniques, micro-emboli distributions post-thrombectomy. Blood flow through the

20   microcirculation is modelled for statistically accurate voxels of brain microvasculature including

21   penetrating arterioles and capillary beds. A novel micro-emboli algorithm, informed by the

22   experimental data, is used to simulate the impact of micro-emboli successively entering the penetrating

23   arterioles and the capillary bed. Scaled-up blood flow parameters – permeability and coupling

1

24   coefficients – are calculated under various conditions. We find that capillary beds are more susceptible

25   to occlusions than the penetrating arterioles with a 4x greater drop in permeability per volume of vessel

26   occluded. Individual microvascular geometries determine robustness to micro-emboli. Hard clot

27   fragmentation leads to larger micro-emboli and larger drops in blood flow for a given number of micro-

28   emboli. Thrombectomy technique has a large impact on clot fragmentation and hence occlusions in the

29   microvasculature. As such, in-silico modelling of mechanical thrombectomy predicts that clot specific

30   factors, interventional technique, and microvascular geometry strongly influence reperfusion of the

31   brain. Micro-emboli are likely contributory to the phenomenon of no-reperfusion following successful

32   removal of a major clot.

2   Author summary

34   After an ischaemic stroke - one where a clot blocks a major artery in the brain - patients can undergo a

35   procedure where the clot is removed mechanically with a stent - a thrombectomy. This reopens the

36   blocked vessel, yet some patients don't achieve blood flow returning to their tissue downstream. One

37   hypothesis for this phenomenon is that the clot fragments into smaller clots (called micro-emboli) which

38   block smaller vessels downstream. However, this can't be measured in patients due to the inability of

39   clinical imaging resolving the micro-scale. We therefore develop a computational model here, based on

40   experimental thrombectomy data, to quantify the impact of micro-emboli on blood flow in the brain

41   after the removal of a clot. With this model, we found that micro-emboli are a likely contributor to the

42   no-reflow phenomenon after a thrombectomy. Individual blood vessel geometries, clot composition,

43   and thrombectomy technique all impacted the effect of micro-emboli on blood flow and should be taken

44   into consideration to minimise the impact of micro-emboli in the brain. Furthermore, the computational

45   model developed here allows us to now build large-scale models of blood flow in the brain, and hence

46   simulate stroke and the impact of micro-emboli on the entire brain.

3   Introduction

48   Stroke is the second largest cause of mortality and of adult disability globally [1]. Ischaemic stroke –

49   the physical occlusion of a cerebral artery by a blood clot (embolus) restricting blood supply to a part

50   of the brain – is the most common form of stroke, occurring in approximately 85% of strokes [1]. Time

51   is critical in stroke, with every hour of delay without treatment causing a loss of neurons equivalent to

52   3-4 years of ageing [2] and a 6% reduction in positive outcome once the patient is treated [3].

53   Since 2015, the use of intra-arterial thrombectomy – the mechanical removal of a clot via a stent – has

54   become the standard of care for patients with acute ischaemic stroke caused by large vessel occlusion

55   [4,5]. Despite this, many patients do not recover full perfusion in their tissue downstream of the

56   recanalized vessel [6]. This observation, commonly known as the "no-reflow" or "no-reperfusion"

57   phenomenon, has been documented in numerous studies involving both animals and humans [7–12].

58   Hypotheses for this phenomenon include: changes in the ultrastructure of the microvasculature and

59   spontaneous blood clotting [7], capillary stalling and leukocyte adhesion [10,13–15], breakdown of the

60   blood-brain barrier leading to tissue swelling and vessel collapse [12,16,17], vasoconstriction of the

61   capillary vessels due to pericyte death [10,18,19], oxidative stress and inflammatory responses [11],

62   and micro-emboli fragments post-recanalization blocking micro-vessels downstream of the clot [8,20].

63   One of the above hypotheses for the no-reflow phenomenon – a micro-emboli "shower" fragmenting

64   off the clot – is of interest due to the clear clinical treatment pathway via thrombolysis. There is indirect

65   evidence that micro-emboli can fragment off clots and lead to worse patient outcomes. Patients who

66   undergo endarterectomy (surgical removal of a plaque in the vasculature) with stenting in the carotid

67   artery are 3 times as likely to have lesions appear in diffusion weighted MRI scans, and have non-

68   disabling strokes, than those who only had an endarterectomy [21]. There is therefore a potential link

69   between clot fragmentation and the potential for microvascular occlusions and worse patient outcomes.

70   As part of the INSIST (*IN-silico clinical trials for treatment of acute Ischaemic STroke*) consortium

71   (www.insist-h2020.eu) we are developing full brain models of blood flow and oxygen transport in

72   health, after an ischaemic stroke, and post-thrombectomy/thrombolysis [22]. The goal of INSIST is to

73   advance in-silico clinical stroke trials for biomedical products for the treatment of ischaemic stroke. As

74   such, an accurate model of clot fragmentation during thrombectomy is required to simulate the effect

75   of micro-emboli on reperfusion post-recanalization. This will help in deducing whether micro-emboli

76   are a major reason for no-reperfusion.

77   Due to the intrinsically microvascular nature of the no-reflow phenomenon, it is impossible to assess

78   the impact of micro-emboli showers in humans, with most microinfarcts being < 1 mm in size making

79   in-vivo detection of them challenging [23]. However, silicone in-vitro models of human cerebral

80   vasculatures have been used to quantify how a clot fragments during thrombectomy using a range of

81   removal techniques and different clot consistencies [20,24]. Most other experimental works analysing

82   the impact of occlusions on the microvasculature come from mouse models [25–28]. Recently, an in-

83   silico study on a mouse cortex microvascular network found that the severity of micro-strokes in the

84   capillary bed were heavily influenced by the local network topology, with decreases in flow of up to

85   80% in the local vicinity of the capillary [29].

86   On the macro-scale, full organ models of blood flow in the brain have been developed [30,31]. These

87   models treat the microvasculature in the brain as a continuous porous medium, effectively smoothing

88   out the local topology and variations in blood flow. Crucially, these models are parameterized by

89   simulations of blood flow in the microvasculature [32]. As such, in order to achieve the aim of

90   simulating a micro-emboli shower in the microvasculature and to determine its effect on the large-scale

91   blood flow, a multi-scale model of micro-occlusions will be developed here. This model will link the

92   blood flow in the microvasculature to the parameters used to model full brain blood flow and the effect

93   of thrombectomy on the microcirculation, both at the penetrating vessel scale and the capillary scale.

94   To the best of our knowledge no models of micro-emboli occlusions have been developed for post-

95   thrombectomy patients.

96   This paper then seeks to answer, through modelling informed by in-vitro experiments, the following

97   questions: To what extent is clot fragmentation responsible for the post-thrombectomy no-reflow

4

98   phenomenon? Can the changes in the blood flow modelling parameters due to micro-emboli showers

99   be accurately quantified such that they can be used in the full organ models? What impact do

100   thrombectomy technique and clot consistency have on downstream blood flow post-thrombectomy?

4 Materials and methods

4.1 Modelling framework

103   In order to investigate the effects of micro-emboli on the cerebral microvasculature, a modelling

104   framework must first be developed. There are two main ways in which the cerebral microvasculature

105   can be modelled – either as a network of individual vessels [35–37], or as an averaged porous medium

106   [30,31,33,38]. We model the microvasculature as a porous medium in order to allow large regions of

107   the brain to be modelled computationally feasibly.

108   The microvasculature will be parameterised following on from previous research developed by our

109   group [32,33,39]. Firstly, statistical models are developed which match morphological properties of the

110   human cerebrovascular network [40–43]. The microvasculature is then split into 2 different spatial

111   scales – the capillary bed, and the penetrating arterioles. In order to scale up the microvasculature to

112   larger regions, the capillary bed blood flow is parameterised with a permeability, as are the penetrating

113   arterioles. The flow from the penetrating arterioles to the capillary bed is parameterised through

114   coupling coefficients – which represent the conductance of the pre-capillary arterioles. The

115   parameterisation method is explained in Section 4.7. Example networks of the different microvascular

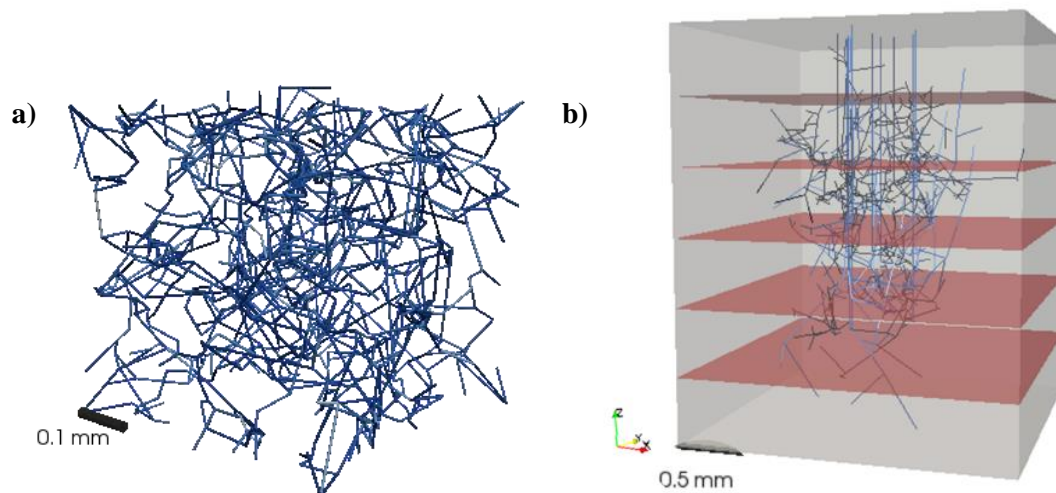116   scales and their coupling can be seen in Fig 1.

117

Fig 1. a) An example of a statistically accurate capillary network, b) An example of a voxel used to simulate flow through the penetrating arterioles. The grey region represents the homogenized capillary bed to which the terminal vessels of the trees couple. The red planes denote the dividing planes between the 6 layers of the voxel over which the blood flow characteristics will be calculated.

4.2 In-vitro emboli quantification

Previous in-vitro studies generated micro-emboli distributions from thrombectomy procedures. In brief, a silicone cerebrovascular model built from clinical imaging data was used in a flow loop with a peristaltic pump to simulate blood flow through the cerebral vasculature [24,44]. A thrombus was injected into the cerbrovascular replica to form a middle cerebral artery (MCA) occlusion. The thrombus was either defined as a soft or hard clot, and validated for bulk mechanical properties based on clinical specimens [45]. Four different clot removal techniques (thrombectomy) were then deployed to remove the clot from the MCA. Specifics on the 4 thrombectomy techniques – abbreviated as ADAPT, Solumbra, BGC, and GC at cervical ICA – can be found in Chueh et al. [20]. The number and size distribution of the clot fragments that break off the thrombus during thrombectomy are quantified using a Coulter counter (Beckman Multisizer 4, Brea, California). Each removal technique is repeated 8 times for each clot type, resulting in 64 sets of clot fragment data.

6

135   When sampling from this data for our in-silico models the 8 experimental micro-emboli density

136   distributions (for a given removal technique and clot type) are averaged such that for any given

137   technique and clot type there is only one average set of micro-emboli results relating number density

138   and particle size. The smallest clot measurable, due to the aperture used in the Coulter counter, was

139   8.034 µm in diameter, with smaller clots binned under this size.

4.3 Simulating blood flow in the microvasculature

141   Prior work has shown how blood flow can be simulated in a coupled model of the penetrating vessels

142   and a porous representation of the capillary bed [33]. This model is adapted here such that it can be

143   used to determine the permeability of the penetrating arterioles in health and with micro-emboli

144   occluding the vessels.

145   An example voxel, where the penetrating arterioles are coupled to the capillary bed, is shown in Fig 1b.

146   Flow through the penetrating vessels is assumed to be steady-state, non-pulsatile (Womersley number

147   << 1) and fully developed, hence approximated by Poiseuille flow:

148

$$q = \frac{\pi R^4 \Delta P}{8 \mu(R) L} \tag{1}$$

149   where q is the blood flow through the vessel, R is the radius of the vessel, ΔP is the pressure drop across

150   that vessel, L is the length of the vessel, and $\mu(R)$ is the apparent viscosity of blood in the vessel

151   correcting for the Fåhræus-Lindqvist effect with a constant discharge haematocrit of 0.45 [46].

152   As flow is conserved at each bifurcation node i, the net flow at each node in the tree is zero except for

153   the one inlet node and the multiple terminal nodes that end in the capillary bed. Therefore, the flow

154   through each internal node for n nodes can be written as:

155

$$\sum_{i=1}^{n} (P_i - P_j) G_{ij} = 0 \tag{2}$$

7

156   where G_{ij} is the flow conductance between nodes i and j and is defined as $\frac{\pi R^4}{8\mu L}$ as in equation (1). The

157   conductance is zero unless there is a vessel between nodes i and j. P_i and P_j are the pressures at nodes

158   i and j respectively. The inlet flow and terminal flows are handled by the boundary conditions at the

159   inlet to the arteriole and at the coupling points to the capillary bed. This set of n equations can be written

160   in matrix form and solved as in Su et al. [47].

161   The capillary bed can be modelled as a porous medium using a volume-averaged form of Darcy's law

162   [32,48]:

163    $$\boldsymbol{u_c} = -K_c \nabla p_c \qquad (3)$$

164   where $\boldsymbol{u_c}$ is the volume averaged capillary velocity, K_c is the permeability (as the permeability is

165   isotropic this can be treated as a scalar), and ∇p_c is the pressure gradient across the capillary bed. The

166   permeability K_c encapsulates the micro-scale geometry of the capillary bed in one averaged parameter,

167   hence allowing for large-scale regions to be modelled computationally efficiently. This equation can be

168   combined with mass conservation to give:

169    $$\nabla . (K_c \nabla p_c) = -S \qquad (4)$$

170   where S is the volumetric source/sink term [m^3 s^{-1} m^{-3}] that comes from the terminal nodes of the

171   penetrating vessels. The healthy capillary permeability value has previously been found be 4.28×10^{-4}

172   mm^3 s^{-1} kg^{-1} [32]. Equation (4) is the Poisson equation that can be solved for capillary pressure over an

173   appropriate 3D domain.

174   **4.4 Coupling penetrating vessels and capillary bed**

175   The coupling between the penetrating vessel terminal nodes and the porous capillary bed has a

176   mathematical singularity at the point of coupling between 1D flow and 3D tissue. Previous models have

177   approximated the Dirac delta singularity with a function that is spatially variant yet maintains mass

178   conservation [30]; have approximated the pressure drop in the vicinity of the coupling point to deal with

179   the strong pressure gradients that appear there [49]; or have simply taken the discretised element nearest

180   the terminal node as the outlet region [33,50]. Here, we use a spatially variant function to approximate

181   the volumetric source terms [30]. A shape function is introduced that replaces the Dirac delta singularity

182   with an exponential in the vicinity of the source. The shape function, η, is defined as

183
$$\eta := \begin{cases} C \, exp\left(\dfrac{1}{\left|\frac{x}{\epsilon}\right|^2 - 1}\right), & \left|\dfrac{x}{\epsilon}\right| < 1 \\[4mm] 0, & \left|\dfrac{x}{\epsilon}\right| \geq 1 \end{cases} \tag{5}$$

184   where x is the distance measured from the source/sink node and ϵ is the radius of the sphere over which

185   the flow will be distributed from the arteriole source to the capillary bed (here set as 15 µm). C is a

186   constant that acts to normalise η to ensure mass conservation across the capillary bed elements coupled

187   to the terminal tree node. Therefore, the volumetric source term for each finite element within ϵ radius

188   of the terminal node will be

189
$$S_k = \sum S * \eta(x - x_k) \tag{6}$$

190   where S_k is the volumetric source term for one element within ϵ radius of the terminal node and x_k is

191   the coordinate of the terminal node. A summation is used to account for the potential that multiple

192   terminal nodes may feed an individual element. As the shape function η conserves mass, $\int \eta(x)dx = 1$

193   and hence $\sum_k S_k = S$.

4.5 Solving for blood flow under healthy conditions

195   The voxel size chosen to simulate the flow is 2 x 2 x 2.5 mm (on the order of an MRI voxel), with 8

196   arterioles /mm^2 penetrating into the voxel [51]. This voxel was situated in a capillary bed of 2.25 x 2.25

197   x 2.5 mm to avoid terminal nodes being at the face of the voxel (Fig 1b). As the parameterisation of

198   micro-emboli occluding the penetrating arterioles was primarily of interest here, the venules were not

199   included in the simulation. As well as this, the permeability of the capillary bed was chosen such that

200   the maximum possible flow could be obtained through the arterioles (in this case K_c was set to 4.2x10^{-5} mm^3 s kg^{-1}). The arterioles have a mean diameter of 20 µm ± 5 µm, with a mean length of 1.25 mm ±

9

202 0.31 mm. An inlet pressure of 12.3 kPa is imposed at the tree inlets [52]. Dirichlet boundary conditions

203 were imposed at the top and bottom of the voxel with $P_{top} = 12.3 \ kPa$ at $z = 0$ and $P_{bottom} = 8 \ kPa$

204 at $z = 2.5 \ mm$, with periodic boundary conditions on the 4 other faces.

205 The finite element method is used to simulate the capillary bed partial differential equation using

206 FEniCS, an open source finite element solver [53]. Equation (4) is solved with the parameters and

207 boundary conditions using 870,000 linear Lagrangian elements to obtain the pressure in the capillary

208 bed. The equations above were solved iteratively. The pseudo-algorithm below details the solution

209 steps:

210 <u>Flow Solver Algorithm</u>

211 1. Set Dirichlet boundary conditions on the top and bottom of the voxel and periodic boundary

212 conditions on the 4 sides;

213 2. For all tree outlets coupled to capillary bed, determine elements in mesh coupled to the outlet

214 node, and determine their η weightings using equation (5);

215 3. Set desired inlet pressures for penetrating vessels and set initial terminal outlet pressures $= 0$

216 4. Solve for the pressure in the trees using equations (1) and (2), hence solve for the outlet flows

217 from the trees into the capillary bed weighting the volumetric source terms using equations (5)

218 and (6);

219 5. Set the volumetric source terms in equation (4) and solve for the capillary bed pressure using

220 the finite element method;

221 6. Update penetrating vessel terminal node pressure values using an η weighted average of the

222 capillary bed pressures related to the given terminal node;

223 7. Go to step 4 and repeat, unless a steady state is reached where pressures in terminal nodes and

224 capillary bed have converged to a tolerance of $1\text{x}10^{-3}$ Pa;

225

4.6 Simulating micro-emboli post-thrombectomy

In order to simulate the effect of micro-emboli on the microvasculature, an algorithm is presented here that samples from the in-vitro experimental thrombectomy data and occludes vessels sequentially. The algorithm flowchart is schematically represented in Fig 2.
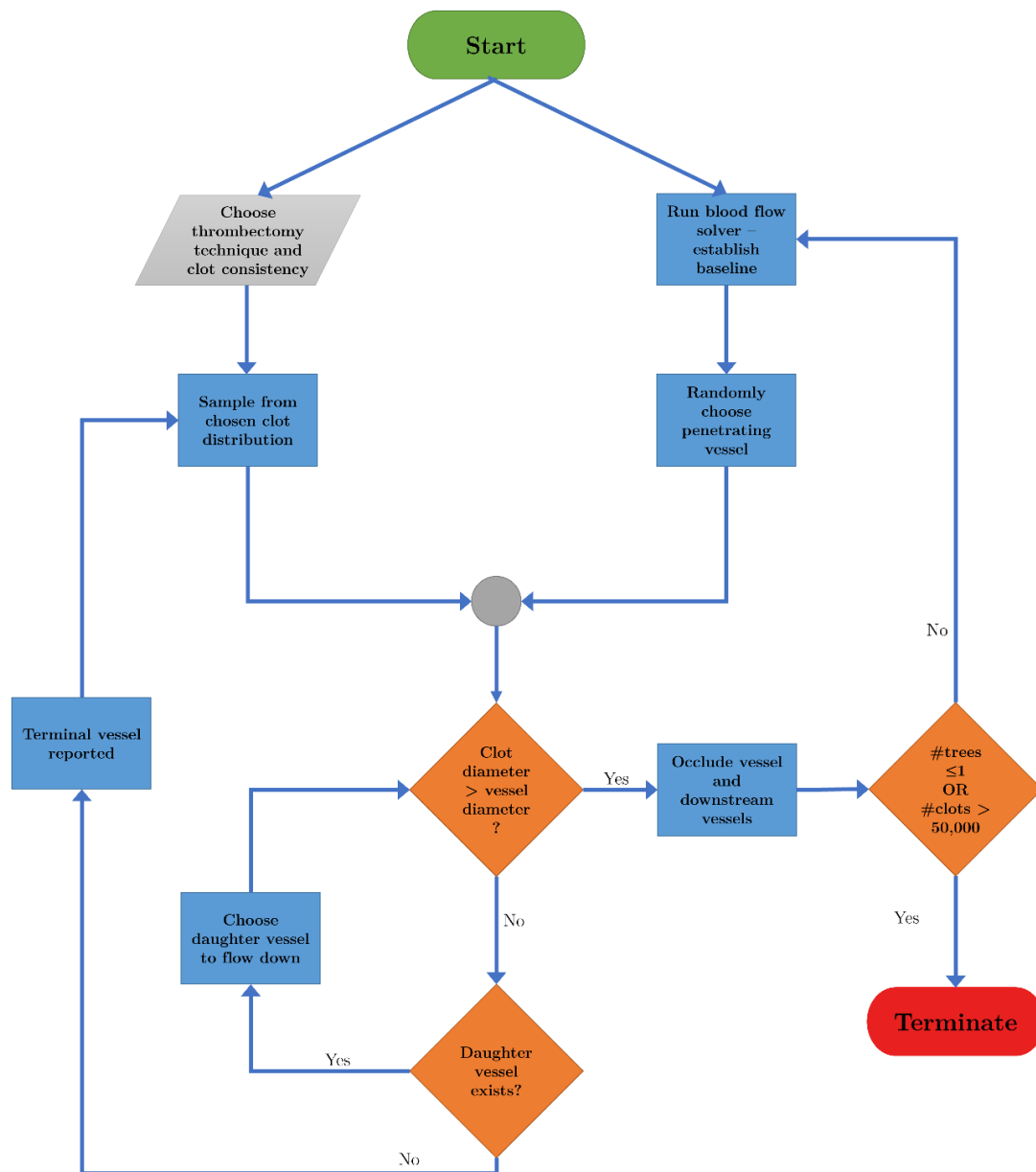

Fig 2. Flowchart representation of the micro-emboli occlusion algorithm

A clot technique and clot consistency are chosen from one of our 8 clot distributions as described in Section 3.2. The algorithm initially runs the healthy flow solver above to establish baseline healthy

11

234   blood flow. A clot size is then sampled pseudo-randomly using Python's inbuilt 'random' module from

235   the experimental distributions derived from the in-vitro models [20].

236   A penetrating arteriole is randomly chosen on the pial surface through which the clot is sent through.

237   The clot is assumed to be perfectly spherical. A check is then made to determine whether the clot is

238   larger than the diameter of the vessel it is entering. If the clot is smaller than the vessel, the clot is

239   assumed to travel until the next bifurcation. At the bifurcation, the clot enters one of the two daughter

240   branches based on a probability that is linearly weighted by the blood flow in the daughter branches.

241   For example, if one daughter vessel has 3 times as much flow as the other daughter vessel, the clot has

242   a 75% chance of going down the vessel with more flow.

243   The clot continues to travel through vessels if its diameter is smaller than the diameter of the vessel it

244   is entering. If the clot enters a vessel with a smaller diameter, it is assumed that the clot completely

245   occludes that vessel. When that occurs, it is assumed no blood can enter the occluded vessels or any

246   vessels downstream of the occluded vessel. The algorithm recalculates a baseline blood flow and

247   resamples a clot to loop through the steps again.

248   If the clot reaches a terminal vessel, and it is still smaller than the vessel, it is assumed that the clot

249   generates no occlusions in the penetrating vessels and enters the capillary bed. As we are trying to

250   quantify the damage done by micro-emboli to the penetrating vessels, we do not create capillary bed

251   occlusions in this simulation. The effect of micro-emboli on the capillary bed is thus considered

252   separately in Section 4.9. As such, no vessels in the penetrating tree are occluded, and a new clot is

253   sampled to loop through the algorithm again.

254   The algorithm described, shown in Fig 2, is repeated until only one penetrating vessel remains or until

255   50,000 clots have been sampled, whichever comes first. The large number of maximum clots is chosen

256   such that we can ensure that all the vessels are eventually occluded, allowing us to track the damage

257   done by micro-emboli sequentially.

258   **4.7 Parameterising the penetrating arterioles**

259   There are 2 specific parameters of interest when attempting to model the penetrating vessels over a

260   large scale – the permeability and the coupling coefficients. The permeability of the penetrating vessels

261   represents the ability of the trees to drive blood flow deeper into the grey cortex due to their 1-

262   dimensional nature [54], and the coupling coefficients represent the pre-capillary arterioles' ability to

263   deliver blood to the capillary bed. These parameters are necessary to simulate large regions of the human

264   brain blood flow efficiently [31]. However, these parameters also effectively average out the micro-

265   scale fluctuations in the vasculature, replacing a complex network with one parameter. This can be

266   problematic with the penetrating vessels when considering, for example, the terminal nodes of the trees.

267   It is highly unlikely they are distributed evenly through the grey matter with depth. It is also highly

268   unlikely that the permeability of the trees is constant with depth through the voxel. We mitigate this

269   problem by splitting the voxel into 6 layers, similar to other approaches [37,55]. Permeabilities and

270   coupling coefficients are then calculated for each of the 6 layers through the voxel, increasing the

271   resolution of the large-scale simulations.

272   **Permeability.** As the permeability of interest is defined as the ability of the penetrating vessels to

273   drive blood flow deeper into the cortex, it is calculated in the vertical direction only. The angle that

274   every vessel makes with the vertical is calculated (situating the vertical at the vessel node where flow

275   enters the vessel). The vertically projected flow of the vessel, $Q_{z,i}$, is then calculated as

276
$$Q_{z,i} = Q_i cos(\phi) \tag{7}$$

277   where ϕ is the angle between the vessel and the vertical, and Q_i is the absolute flow through the vessel.

278   The arterial blood flow, $Q_{z,i}$, through each of the six layers is then summed separately and the

279   permeability calculated as

280
$$K_{a,l} = \frac{Q_l}{\Gamma_z \nabla P_l} \tag{8}$$

13

281   where $Q_l = \sum Q_{z,i}$ through layer l, $K_{a,l}$ is the arteriolar permeability in layer l, Γ_z is the cross-sectional

282   area through which the blood flows (in this case the area of the voxel), and ∇P_l is the pressure gradient

283   across the layer. Using this method provides 6 different estimates of arteriolar permeability at 6 different

284   depths in the grey matter.

285   **Coupling coefficients.** The method to calculate the coupling coefficients can be found in Hyde et al.

286   [56]. The coupling coefficients can be thought of as a conductance (or 1/resistance) to flow from the

287   arteriolar compartment to the capillary compartment via the pre-capillary arterioles. This can be written

288   as

$$Q_t = \beta_{ac}(\langle p_a \rangle - \langle p_c \rangle) \tag{9}$$

290   where β_{ac} is the coupling coefficient between the arteriolar and capillary compartments, $\langle p_i \rangle$ is the

291   volume averaged pressure of compartment i, and Q_t is the flow of the arterioles which terminate in the

292   capillary compartment. This can be rewritten as

$$\beta_{ac}(l) = \frac{Q_t(l)}{|\langle p_a(l) \rangle - \langle p_c(l) \rangle|} \tag{10}$$

294   where the bracket l term refers to the values in layer l. The volume averaged flow in layer l, $Q_t(l)$, can

295   be calculated using equation (1). The volume averaged pressure of the arteriolar compartment $\langle p_a(l) \rangle$

296   is calculated via

$$\langle p_a(l) \rangle = \frac{\sum_{n,l} P_n V_n}{\sum_{n,l} V_n} \tag{11}$$

298   where P_n is the average nodal pressure of vessel n in layer l, and V_n is the volume of vessel n in layer

299   l. Six values of average pressure are calculated, one for each layer.

300   Finally, the volume averaged capillary pressure at each layer $\langle p_c(l) \rangle$ is calculated by taking the volume

301   average of the pressures in the finite element mesh of the capillary bed. This allows for the permeability

302   and coupling coefficients of the penetrating vessels to be fully characterised. In order to be able to

303   characterise the variable permeabilities and coupling coefficients calculated above, a polynomial least

304   squares fit is used to derive a function of how these coefficients vary with depth which is then fitted

305   over the 100 simulations conducted on the statistically accurate voxels.

4.8 Investigating thrombectomy technique, clot composition, and individual microvasculatures

308   Based on the pipeline previously presented, we now seek to investigate whether the different micro-

309   emboli distributions from thrombectomy have an impact on the permeability (and hence perfusion) of

310   the penetrating arterioles following the introduction of micro-emboli. The micro-emboli algorithm is

311   therefore used to simulate an emboli shower for 8 different scenarios – 4 techniques used on 'hard' or

312   'soft' clots.

313   As well as this, we investigate the impact that differing microvasculatures have on the resulting drops

314   in permeability and coupling coefficients. Each of the 100 statistically accurate voxels can be thought

315   of as an 'individual' microvasculature. We randomly choose 3 of these voxels and, for each voxel, we

316   simulate 100 different sampled clot distributions entering the penetrating vessels. These simulations are

317   compared to another simulation where we take our 100 voxels and run the same sampled clot

318   distribution through each voxel – this is done for 3 different sampled clot distributions. The question

319   that we seek to answer is whether it is the microvasculature or the clot distributions that primarily

320   determine microvascular robustness to drops in perfusion. Differences between distributions are

321   quantified using the correlation matrix distance (CMD) on the covariance matrices of each distribution

322   [57].

4.9 Micro-occlusions in the capillary bed

324   Finally, the effect of micro-emboli on capillary beds is considered. Previously, we demonstrated how

325   statistically accurate models of capillary beds can be homogenized into a porous medium [32]. This

326   method is combined here with a vessel occlusion algorithm to simulate the effect of micro-emboli

327   entering the capillary bed. The decrease in permeability as a function of the vessel fraction lost, surface

15

328   area fraction lost, and volume fraction lost are all quantified. This allows for the scaling up of partially

329   occluded capillary networks to large regions of tissue.

330   Details of the blood flow simulation and homogenization of the capillary bed can be found in El-Bouri

331   & Payne [32]. In brief, Poiseuille flow is assumed through the capillary vessels, with the capillary

332   network being periodic. A pressure gradient is imposed in one direction and the permeability – the ratio

333   of the volume-averaged flow and the pressure gradient – is calculated. This is repeated for the 3

334   principal directions of the capillary network. The result is a 3x3 tensor, with 3 principal permeabilities

335   (the permeability in the direction of the pressure gradient) and 6 cross-permeabilities.

336   As the smallest measurable clot was 8.034 µm, and the average diameter of a capillary is 6.23 ± 1.3 µm

337   [40], the micro-emboli algorithm above could not be used on the networks as they would always occlude

338   the inlet vessel. As such, a random vessel was chosen in the network and this vessel was fully occluded,

339   with the permeability being recalculated after every occlusion. Three cube sizes were used to simulate

340   the micro-occlusions with lengths of 375, 500, and 625 µm. Normalised permeability changes are

341   calculated, and the effect of the micro-emboli on the capillary bed is quantified such that it can be used

342   in full-brain simulations. Constrained least squares optimization is used to fit a line of best fit with the

343   equation

$$P_f = 1 + Bx_i \qquad\qquad (12)$$

344

345   where P_f is the permeability fraction, x_i is the change in either vessel fraction, volume fraction, or

346   surface area fraction of the networks, and B is the gradient. All parameters calculated for the capillary

347   bed are based on 500 statistically accurate capillary networks at each cube size (1500 total).

5   Results

5.1 Healthy blood flow in the penetrating arterioles

Blood flow was simulated in 100 statistically accurate voxels of the cerebral microvasculature. The permeability and coupling coefficients were quantified for the penetrating arterioles in the 'no-occlusion' scenario. The permeability results are shown in Fig 3.
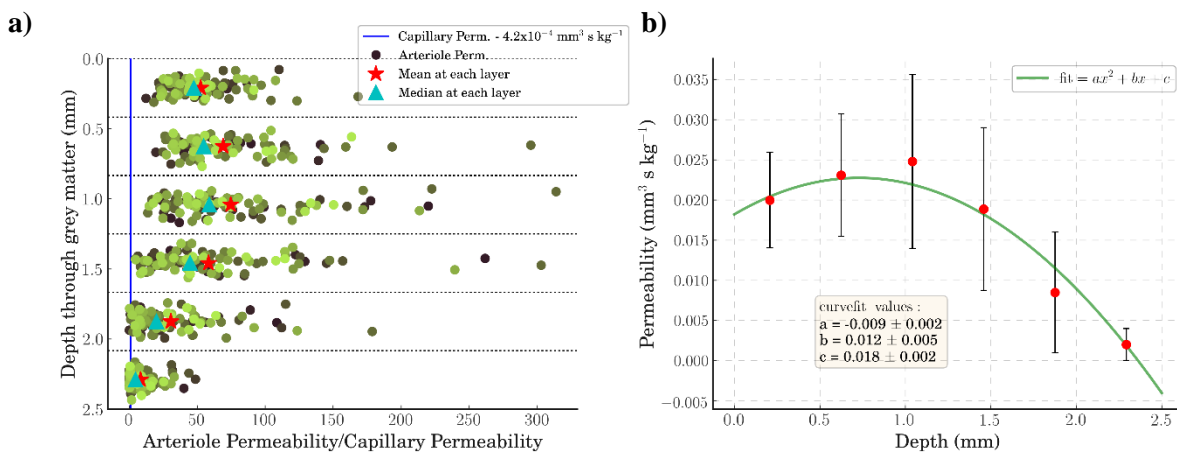

Fig 3. a) A scatter plot of the permeability of the 100 voxels at each of the 6 depth layers. The cyan triangle indicates the median permeability of the capillary bed. The mean arteriolar permeability is indicated with a red star at each layer. b) A quadratic line of best fit over the median permeabilities at each layer – error bars are interquartile ranges

The permeability increases with depth until the middle layers before dropping off towards the bottom layers, as not all penetrating vessels penetrate the full depth of the grey matter (Fig 3a). The mean value of the permeability across the layers is approximately 50 times the capillary permeability. At each layer the average permeability ranges from around 30x at the top layer, to 75x in layer 3, to 9x at the bottom layer. A quadratic curve fit is used to derive a function that models arteriolar permeability with depth, such that it can be used in future porous model implementations (Fig 3b). The permeability distribution at each layer can also be characterised as log-normal (Shapiro-Wilks test, $\alpha = 0.05$) up to and including layer 4 (S1 Table).

17

366   The coupling coefficients demonstrate a similar drop from the top layers to the bottom layers, driven

367   by the fact that there are fewer terminal nodes at the bottom layers [33]. The variability in the coupling

368   coefficients from voxel-to-voxel is larger than the permeability variability (S1 Fig). The median values

369   of the coupling coefficients are 2.8×10^{-5}, 4.4×10^{-5}, 4.3×10^{-5}, 2.7×10^{-5}, 1.1×10^{-5}, and 4.3×10^{-6} Pa^{-1} s^{-1}

370   (from layers 1 – 6). A quadratic curve-fit is used to derive a function that models the coupling

371   coefficients with depth for future porous model implementations (S1 Fig). The coupling coefficient

372   distribution can be characterised as log-normal (Shapiro-Wilks test, $\alpha = 0.05$) up to and including layer

373   4 (S2 Table).

374   The above results parameterise the healthy penetrating vessels so they can be scaled up to large regions

375   of the brain. More importantly, however, these healthy results provide a baseline from which the effect

376   of micro-occlusions can be quantified.

5.2 The arterioles are robust to micro-emboli at the population level

378   As there are 4 thrombectomy techniques used with 2 clot consistencies to give 8 different micro-emboli

379   distributions to choose from, a baseline must be chosen to conduct the following simulations. Here we

380   choose the ADAPT technique with a hard clot to present the following results. A comparison with other

381   techniques and clot consistencies can be found in Sections 5.4, 5.5.

382   The variable of interest here is the fractional drop in permeability. This is defined as the permeability

383   divided by the initial healthy permeability. We compare this independent variable against 3 dependent

384   variables – the fraction of vessels occluded, the fraction of vessel surface area occluded, and the fraction

385   of vessel volume occluded. The surface area and volume drops have been calculated as these geometric

386   parameters control oxygen transport in the microvasculature and can in future be used for validation.

387   Fig 4 shows these results for 2 different layers – the top-most grey matter layer, and the middle layer

388   (from 1.25 – 1.67 mm depth). An example of the permeability decrease against volume fraction decrease

389   in all 6 layers can be found in S2 Fig.
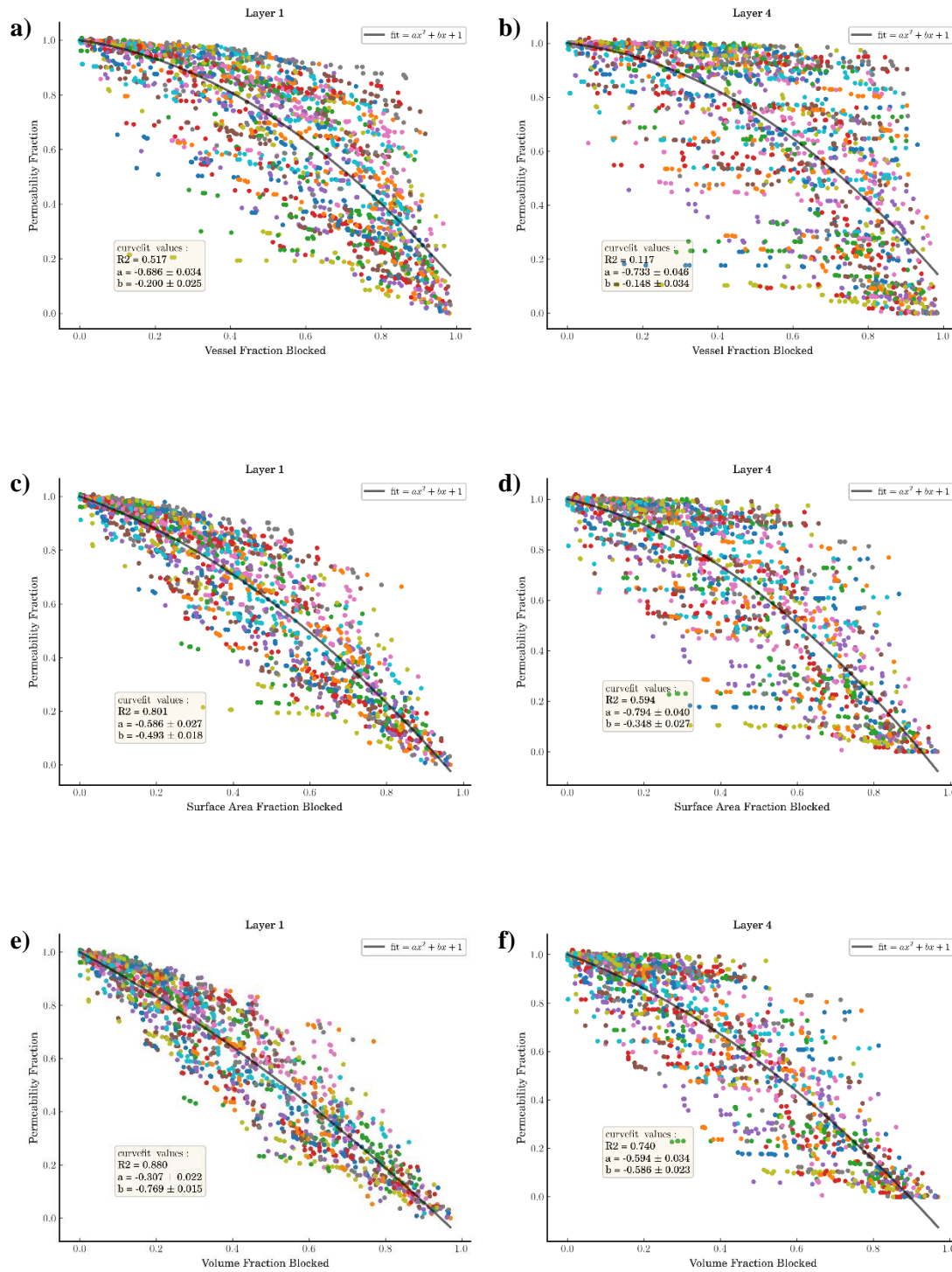
390

391

392

Fig 4. a,b) The fractional drop in permeability against the fraction of vessels blocked where a) is

in the top layer of the voxel and b) is the middle layer. c,d) The fractional drop in permeability

against the fraction of vessel surface area blocked where c) is in the top layer of the voxel and d)

is the middle layer. e,f) The fractional drop in permeability against the fraction of vessel volume

397   **blocked where e) is in the top layer of the voxel and f) is the middle layer. The middle layer is at**

398   **a depth of 1.25 – 1.67mm. A line of best fit is plotted in black, with the fit equation in the top right**

399   **corner of each graph, with the bottom left of the graph giving the coefficients of the line of best**

400   **fit and the R^2 goodness-of-fit metric.**

401   The permeability is generally robust with vessel fraction blocked, up to around 50 % of the vessels

402   before the permeability starts to drop more rapidly. This can be explained by the fact that many small

403   vessels are occluded first – due to 98% of all emboli having a diameter of $< 20\,\mu$m for this configuration

404   of clot consistency and thrombectomy technique – which has a relatively small impact on the

405   permeability. On the other hand, the permeability drops almost linearly with volume fraction blocked

406   with a 1:1 ratio in the top layer.

407   Interestingly, in the middle layer for all 3 dependent variables, the permeability's robustness to

408   occlusions appears to improve over the first 40-50% of vessel/volume occlusions. As the vessels

409   continue to be occluded, however, the drop off in permeability is quicker than in the topmost layers.

410   The variability increases with depth until by the time the bottom two layers are reached, there is almost

411   a dichotomous choice between a permeability of 1 and 0 (S2 Fig). This is due to the sparse number of

412   vessels in the lower layers, leading to them being vulnerable to very few micro-emboli.

413   The permeability, and its drops with successive micro-emboli, can thus be characterised as a 2-

414   dimensional surface. The equation for the healthy permeability distribution with depth can be

415   multiplied, at each depth layer, by the respective permeability drop equation for that depth layer. An

416   example of a 2-dimensional surface generated with volume fraction as the dependent variable, ADAPT

417   as the thrombectomy technique, and a hard clot can be found in Fig 5 (calculated using the healthy

418   permeability equation from Fig 3b). These 2-dimensional functions can be calculated for all the

419   different possible combinations of thrombectomy, clot, and dependent variable. This provides a simple

420   look-up table to determine the change in permeability for a given technique, clot, depth, and fraction
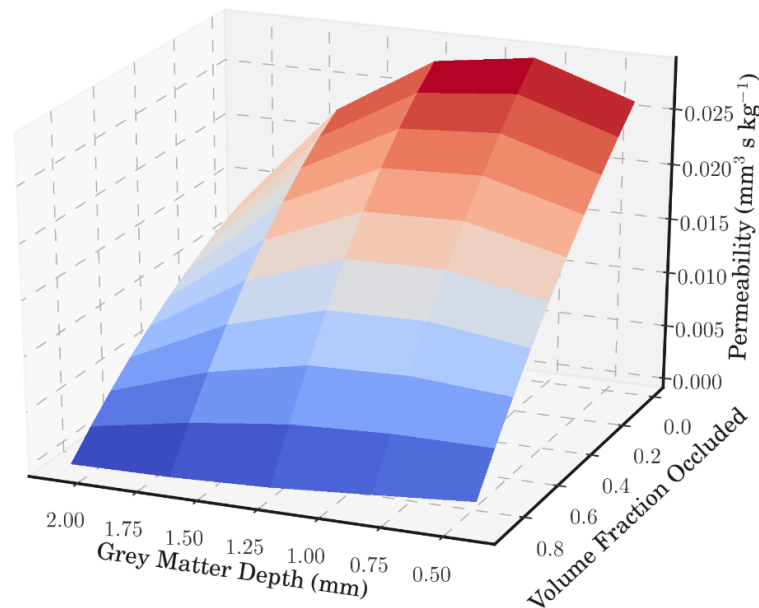
421   occluded.

Fig 5. A 2-dimensional surface plot for the ADAPT thrombectomy technique removing a hard clot. The permeability is plotted against voxel depth and volume fraction of the vessels occluded.

The coupling coefficients also display non-linear behaviour with micro-emboli occlusions, but this behaviour is far more variable than the permeability results. This is due to blood being rerouted as occlusions occur, leading to coupling coefficients increasing as well as decreasing from the baseline. As well as this, the coupling coefficients are also dependent on the pressure in the capillary beds and terminal arterioles (Eq (10)). An example of the change in coupling coefficients with depth and volume occlusions can be found in S3 Fig.

5.3 The microvascular geometry dictates robustness to micro-emboli smaller than the penetrating vessel inlet diameter

To investigate the role of the microvasculature on robustness to micro-emboli, 3 voxels were chosen from our 100 voxels. Each voxel had 100 micro-emboli simulations with each simulation having a different clot distribution sampled. Fig 6 shows the changes of permeability for these 3 voxels for the middle-layer. As can be seen, it appears that the microvascular topology dictates the response to micro-emboli, with clear banded regions with non-linear jumps for some voxels, whilst other voxels have an almost linear drop with increasing occlusions.
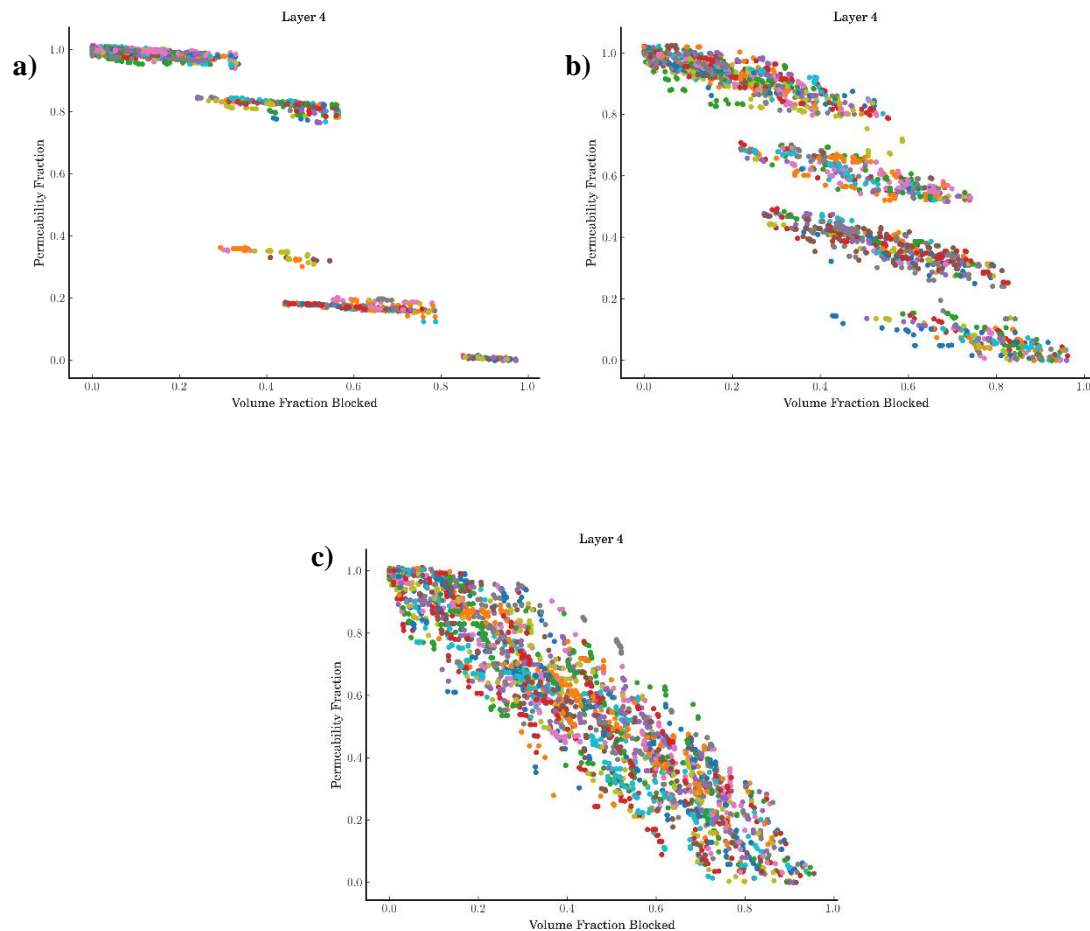
21

439

440

Fig 6. A comparison of the permeability drop against volume fraction occluded for 3 different voxel geometries simulated with 100 different clot distributions (for the ADAPT technique, hard clot) a) Voxel 1, b) Voxel 4, c) Voxel 31

In comparison, we simulated 100 different voxels but with the same sampled clot distribution entering each voxel (we fix the random seed sampling the clot distribution to be the same for each voxel). The aim of this was to investigate the effect of the sampled clot distribution variability on perfusion characteristics (similar to how we investigated the effect of microvascular variability in Fig 6). There was little visual difference found for the 3 sampled clot distributions (S4 Fig). Similar behaviour is also seen for the coupling coefficients, with linear drops in coupling coefficients seen for some voxels (S5 Fig).

22

451   Quantifying the statistical differences between these distributions was complicated by the bivariate

452   nature of the distributions. As such, to provide a simple comparison, we use the correlation matrix

453   difference (CMD) to compare the covariances of each distribution against the baseline distribution

454   (Fig 4f). The CMD has a value of 0 when the covariance matrices are identical and a value of 1 when

455   they are orthogonal. When comparing the 3 constant microvascular simulations the range of the CMD

456   was 1×10^{-4} to 2.85×10^{-3}. For the constant clot simulations, the range was 7×10^{-6} to 3×10^{-4} indicating

457   that variability and robustness to micro-emboli is dominated by the microvascular geometry.

5.4 Hard clot micro-emboli lead to larger drops in permeability

459   The above analysis has all been conducted using 'hard' clot fragmentation data. We now simulate 'soft'

460   clot fragmentation and the effect of these micro-emboli on flow characteristics. We are interested to

461   observe whether clot consistency impacts downstream flow post-thrombectomy.

462   Visually, there is no discernible difference for the relationship between permeability and the dependent

463   variable on the population level, but certain voxels display changes in their permeability relationship

464   (S6 Fig). Comparing individual microvascular geometries in both hard and soft clot simulations, the

465   CMD score ranges between 3×10^{-4} and 7×10^{-3}, indicating a similar variability to that found between

466   voxel comparisons. The results are similar for the coupling coefficients.

467   Regardless of whether there was a visual difference or not, all voxels with soft clot simulations required

468   on average twice as many occluding clots to develop the same drops in perfusion as for the hard clots.

469   As well as this, around 4.5% of the clots sampled from the hard clot distributions went into occluding

470   penetrating vessels (the rest passed through the arterioles into the capillary bed). For the soft clots, this

471   was only 2.5% (Table 1). Clearly, for a given number of micro-emboli the smaller clot fragments of the

472   soft clot lead to smaller drops in permeability.

473   **Table 1. Summary of the differences between thrombectomy technique and clot consistency when**

474   **considering total micro-emboli sampled and those micro-emboli that occlude vessels. The values**

23

475 **are averaged over the 100 voxel simulations. The percentage of sampled clots occluding vessels is**

476 **the average of the 100 individual percentages.**

Thrombectomy Technique	Clot Consistency	Average number micro-emboli sampled	Average number micro-emboli occluding vessels	Percentage of sampled clots occluding vessels (%)
ADAPT	Hard	616.1	24.3	4.5
ADAPT	Soft	2704	48.1	2.5
BGC	Hard	208.5	25.8	14.0
BGC	Soft	994	26.4	3.0
GC at cervical ICA	Hard	1152.7	29.0	2.9
GC at cervical ICA	Soft	1146.6	22.9	2.3
Solumbra	Hard	76.4	18.6	26.3
Solumbra	Soft	1720.2	36.3	2.6

477 **5.5 Thrombectomy technique has a large impact on clot fragmentation and downstream**

478 **flow characteristics**

479 The last variable of interest here is the thrombectomy technique. In the in-vitro experiments, 4

480 techniques were used; these are abbreviated as ADAPT, BGC, GC at cervical ICA, and Solumbra [20].

481 The emboli distributions from these 4 techniques used on hard and soft clots were used to simulate

24

482   occlusions in the penetrating vessels. The results are shown in Fig 7 where the scatter plots have been

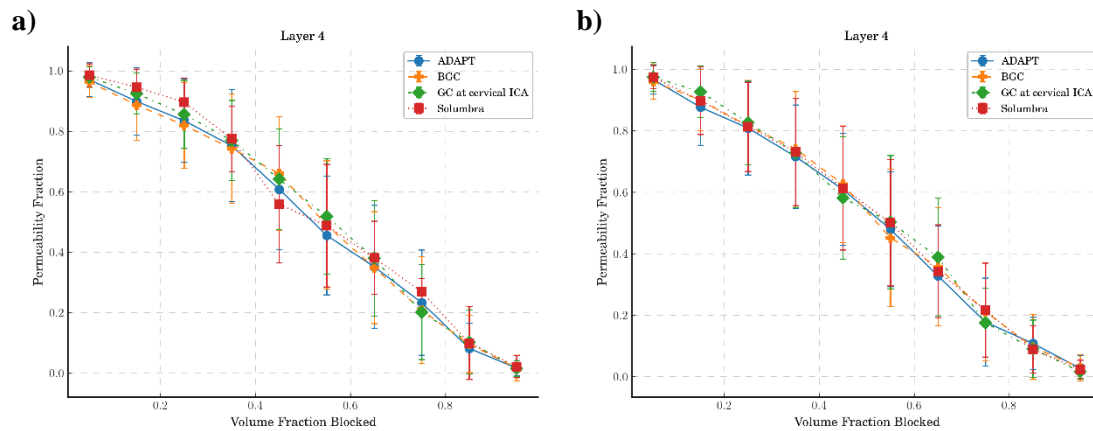483   binned into deciles with mean and standard deviation for ease of viewing.

485   **Fig 7. Comparison of the permeability drops against volume fraction blocked in the middle layer**

486   **for 4 different thrombectomy techniques: a) removing hard clots and b) removing soft clots**

487   Despite there being little visual difference between the 4 techniques, when analysing the numbers of

488   clots required to reach similar drops in permeability, large differences emerge (summarised in Table 1).

489   We measured: the average number of micro-emboli sampled in total to fully occlude the voxel (column

490   3 of Table 1); the average number of these micro-emboli that occlude a penetrating vessel (column 4 of

491   Table 1); and hence the percentage of sampled clots that occluded the penetrating vessels (column 5 of

492   Table 1). Simulating the Solumbra technique on a hard clot resulted in the fewest clots required to fully

493   occlude the voxel; on average over the 100 voxels 18.6 clots (and hence 26% of sampled clots) sent

494   through the penetrating vessels were required to fully occlude the voxel. The BGC technique had the

495   next fewest clots required with 26 clots and 14% of the sampled clots. The GC at cervical ICA

496   technique, on the other hand required 29 clots and 2.9% of the sampled clots.

497   In contrast, when using the soft clots, the numbers of clots required to achieve similar permeability

498   drops drastically increased – except for GC at cervical ICA which had similar results compared to when

499   using the hard clots. Both the Solumbra and ADAPT techniques saw a doubling of the clots required.

25

500   Clearly, there is a trade-off between the number of emboli that fragment off a clot, the size of these

501   emboli, and the impact they have on downstream flow. The BGC and Solumbra techniques were

502   previously reported to minimise the fragmentation of hard clots [20], but this also means that these clots

503   are larger and hence more prone to occlude larger vessels (as indicated by our large percentage of clots

504   that occlude vessels in the above results). On the other hand, the ADAPT and Solumbra techniques used

505   on soft clots lead to twice as many clots being required to occlude the penetrating vessels to achieve

506   similar drops in permeability.

5.6 Occlusions in the capillary bed lead to large drops in permeability

508   Finally, we simulated micro-emboli occluding capillary bed networks. These were simulated for 500

509   statistically accurate networks at 3 different cube length sizes (375 µm, 500 µm, and 625 µm). As the

510   results were not statistically different over the 3 sizes, only the 375 µm results are presented in Fig 8.

511   The permeability maintained its isotropy in the presence of micro-emboli hence it is presented here as

512   a scalar.

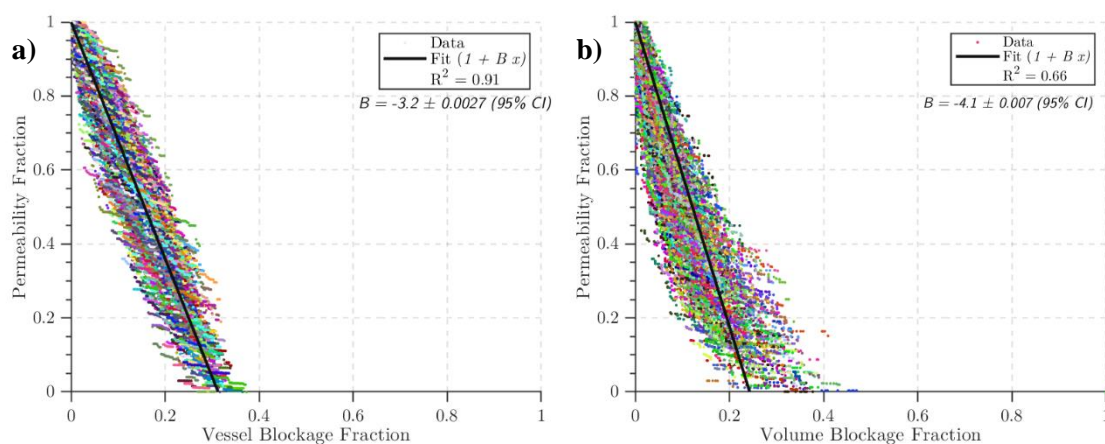**Fig 8. The drops in permeability over 500 statistically accurate capillary networks with a cube length of 375 µm. Lines of best fit are in black, with the gradient B in the top right corner of each graph. a) The fractional drop in permeability with fraction of vessels occluded ($B = -3.2$), b) the fractional drop in permeability with vessel volume occluded ($B = -4.1$).**

26

518 The permeability drop in the capillary bed was large in comparison to the drop in the penetrating vessels:

519 -8 % / % surface area lost, -3.2 % / % vessel blocked, and -4.1 % / % volume blocked (see Fig 8). This

520 is in line with a previous study where a -2.5 % drop in CBF/ % vessels blocked was found in simulations

521 of occlusions in mouse and human vascular networks, as well as mouse synthetic networks [13]. It

522 should be noted that the synthetic networks used in [13] had uniform diameter and length, unlike the

523 networks in this paper which have length and diameter distributions that match physiological

524 distributions.

525 Assuming a micro-emboli shower is spread evenly over the MCA territory (approx. 100 mL of tissue),

526 1.5% of this volume is capillary vessels, and a vessel density of 8000 vessels/mm^3, around 120,000

527 micro-emboli would have to enter the capillary bed to cause a 4% drop in permeability (note that this

528 is an overestimate as micro-emboli are not likely to spread evenly over the brain tissue). Depending on

529 thrombectomy technique, the number of micro-emboli fragmenting off the clot can vary from a few

530 thousand to over 500,000 [20]. It therefore appears that if micro-emboli enter the capillary bed there is

531 significant potential for damage and large drops in perfusion.

532 ## 6   Discussion

533 We return to the questions posed at the end of the introduction. First, can the changes in the blood flow

534 modelling parameters due to micro-emboli showers be accurately quantified such that they can be used

535 in the full organ models? Using a combination of in-vitro experiments of clot fragmentation and in-

536 silico blood flow modelling, we have developed simulations of micro-emboli occluding vessels in the

537 penetrating arterioles and capillary bed. Using these models we characterised 'averaged' flow

538 parameters, such as permeability and coupling coefficients, in healthy conditions and under micro-

539 emboli showers, for a range of thrombectomy techniques and clot consistencies. This now enables us

540 to simulate the impact of these micro-emboli showers – after a thrombectomy – on the downstream

541 tissue and its potential contribution to the 'no-reperfusion' phenomenon.

542   Second, what impact do thrombectomy technique and clot consistency have on downstream blood flow

543   post-thrombectomy? Clot consistency and thrombectomy techniques have been shown here to have a

544   large impact on the blood flow parameters. Whilst the relationship between permeability and volume

545   of vessel occluded was similar, the numbers of micro-emboli required were substantially different, with

546   soft clots on average requiring twice as many micro-emboli to reach similar drops in permeability. The

547   Solumbra and BGC techniques used on hard clots resulted in larger micro-emboli entering the

548   microvasculature, and hence fewer vessels needing to be occluded to reach large drops in permeability.

549   Therefore, whereas the Solumbra and BGC techniques result in fewer emboli fragmenting off the clot

550   [20], these emboli can cause more damage to the microvasculature due to their larger sizes.

551   In addition to this we investigated the impact of microvascular morphometry on blood flow parameters.

552   Microvascular morphometry determined the robustness of penetrating vessels to occlusions, not the

553   sampled micro-clot distribution. Therefore, if we can measure the microvasculature, even if only

554   indirectly, we can determine whether the microvasculature will be robust to a micro-emboli shower.

555   Characterising the microvasculature and its robustness, e.g. through the residue function [34], will be

556   the subject of future work.

557   Finally, we compared drops in permeability for the penetrating vessels and capillary bed. Whilst the

558   penetrating vessels had an approximately 1:1 relationship between volume lost and permeability drop,

559   the capillary bed lost 4% of permeability per 1% volume drop. This lack of robustness to occlusions in

560   the capillary bed is surprising but has previously been reported elsewhere with capillary stalling in

561   mouse capillary beds. In blood flow simulations, Cruz-Hernandez et al. found that for every 1% of

562   vessels stalled, the flow drops by 2.5% [13]. Our results indicate a 3.2% drop in permeability (a

563   surrogate for flow) for every 1% of vessels blocked, which show good agreement for early studies.

564   Permeability is a more robust metric than CBF here due to CBF being dependent on the volume of

565   tissue simulated. As well as this, Schmid et al. found that the severity of a micro-occlusion in the

566   capillary bed depends on the connectivity and original flow rate of the occluded vessel, with large

567   reductions in flow for specific types of connectivities [29]. As we found for the penetrating vessels,

568   morphometry of the microvasculature plays a large role in robustness to micro-occlusions.

28

569   The smallest micro-emboli sizes available from our experimental data were 8 µm. While this was

570   sufficient for micro-emboli occlusions in the penetrating vessels, we did not have information on

571   smaller micro-emboli that would occlude the capillary vessels. This meant we could not track emboli

572   through the capillary bed. In future, data on micro-emboli < 8 µm in diameter would help in more

573   clearly understanding how micro-emboli affect the capillary bed. The diameters measured were the

574   Feret diameters of the micro-emboli, however we used these diameters to assume spherical micro-

575   emboli. It is therefore possible that our drops in permeability are over-estimated, as the clot could orient

576   along a smaller dimension and pass through the vessel.

577   It should be noted that a limitation of the analysis presented here is the separate treatment of the

578   penetrating arterioles and capillary bed. This was done for two reasons. Firstly, to provide a comparison

579   to previous studies, as discussed above. Primarily, however, this was done to fit into our full brain

580   modelling framework where the capillary bed and penetrating arterioles are treated as separate

581   compartments coupled together via coupling coefficients. The effects of extravasation of the micro-

582   emboli in the capillary bed have also been neglected, and these will likely result in restoration of flow

583   over several days [28]. This model is also purely passive, with no hyperaemia or regulation of vascular

584   tone, which likely impact passage of micro-emboli through the microvasculature.

585   The final question posed was: To what extent is clot fragmentation responsible for the post-

586   thrombectomy no-reflow phenomenon? We only analysed the impact of micro-emboli in voxels, or

587   cortical columns of microvasculature. In order to fully understand the impact of micro-emboli on the

588   vasculature, a full brain simulation is required. In future, we will use the work developed here to

589   simulate micro-emboli showers in a full-brain in-silico simulation of thrombectomy. Blood flow

590   parameters in the full-brain model will be updated using the parameters derived here, and the impact of

591   micro-emboli in a region of the brain can be compared and validated against CT perfusion and MR

592   scans of patients pre- and post-thrombectomy. Furthermore, we will investigate further the impact of

593   microvascular morphometry on blood flow drops and how this can potentially be used to infer patient

594   robustness to micro-emboli.

29

7   References

595

596 1.   Owens Johnson C, Nguyen M, Roth GA, Nichols E, Alam T, Abate D, et al. Global, regional, and national

597   burden of stroke, 1990-2016: a systematic analysis for the Global Burden of Disease Study 2016. 2019;

598   doi:10.1016/S1474-4422(19)30034-1

599 2.   Saver JL. Time is brain - Quantified [Internet]. Stroke. Lippincott Williams & Wilkins; 2006. pp. 263–

600   266. doi:10.1161/01.STR.0000196957.55928.ab

601 3.   Fransen PSS, Berkhemer OA, Lingsma HF, Beumer D, van den Berg LA, Yoo AJ, et al. Time to

602   Reperfusion and Treatment Effect for Acute Ischemic Stroke: A Randomized Clinical Trial. JAMA

603   Neurol. United States; 2016;73: 190–196. doi:10.1001/jamaneurol.2015.3886

604 4.   Berkhemer OA, Fransen PSS, Beumer D, van den Berg LA, Lingsma HF, Yoo AJ, et al. A Randomized

605   Trial of Intraarterial Treatment for Acute Ischemic Stroke. N Engl J Med. Massachusetts Medical Society;

606   2014;372: 11–20. doi:10.1056/NEJMoa1411587

607 5.   Jovin TG, Chamorro A, Cobo E, de Miquel MA, Molina CA, Rovira A, et al. Thrombectomy within 8

608   Hours after Symptom Onset in Ischemic Stroke. N Engl J Med. Massachussetts Medical Society;

609   2015;372: 2296–2306. doi:10.1056/NEJMoa1503780

610 6.   Behme D, Tsogkas I, Colla R, Gera RG, Schregel K, Hesse AC, et al. Validation of the extended

611   thrombolysis in cerebral infarction score in a real world cohort. PLoS One. Public Library of Science;

612   2019;14. doi:10.1371/journal.pone.0210334

613 7.   Ames A 3rd, Wright RL, Kowada M, Thurston JM, Majno G. Cerebral ischemia. II. The no-reflow

614   phenomenon. Am J Pathol. 1968;52: 437–453.

615 8.   Molina CA. Reperfusion Therapies for Acute Ischemic Stroke: Current Pharmacological and Mechanical

616   Approaches. Stroke. 2011;42: S16–S19. doi:10.1161/STROKEAHA.110.598763

617 9.   Kurre W, Vorlaender K, Aguilar-Perez M, Schmid E, Bäzne H, Henkes H. Frequency and relevance of

618   anterior cerebral artery embolism caused by mechanical thrombectomy of middle cerebral artery

619   occlusion. Am J Neuroradiol. American Journal of Neuroradiology; 2013;34: 1606–1611.

620   doi:10.3174/ajnr.A3462

621   10.   Kloner RA, King KS, Harrington MG. No-reflow phenomenon in the heart and brain. Am J Physiol Hear

622   Circ Physiol. 2018;315: 550–562. doi:10.1152/ajpheart.00183.2018.-The

623   11.   Bai J, Lyden PD. Revisiting cerebral postischemic reperfusion injury: New insights in understanding

624   reperfusion failure, hemorrhage, and edema. International Journal of Stroke. Blackwell Publishing Ltd;

625   2015. pp. 143–152. doi:10.1111/ijs.12434

626   12.   Mohamed Mokhtarudin MJ, Payne SJ. Mathematical model of the effect of ischemia-reperfusion on brain

627   capillary collapse and tissue swelling. Math Biosci. Elsevier Inc.; 2015;263: 111–120.

628   doi:10.1016/j.mbs.2015.02.011

629   13.   Cruz Hernández JC, Bracko O, Kersbergen CJ, Muse V, Haft-Javaherian M, Berg M, et al. Neutrophil

630   adhesion in brain capillaries reduces cortical blood flow and impairs memory function in Alzheimer's

631   disease mouse models. Nat Neurosci. Nature Publishing Group; 2019;22: 413–420. doi:10.1038/s41593-

632   018-0329-4

633   14.   Erdener ŞE, Tang J, Kılıç K, Postnov D, Giblin JT, Kura S, et al. Dynamic capillary stalls in reperfused

634   ischemic penumbra contribute to injury: A hyperacute role for neutrophils in persistent traffic jams. J

635   Cereb Blood Flow Metab. SAGE Publications Ltd STM; 2020; 0271678X20914179.

636   doi:10.1177/0271678X20914179

637   15.   Ritter LS, Orozco JA, Coull BM, McDonagh PF. Leukocyte accumulation and hemodynamic changes in

638   the cerebral microcirculation during early reperfusion after stroke. Stroke. Lippincott Williams and

639   Wilkins; 2000;31: 1153–1161. doi:10.1161/01.STR.31.5.1153

640   16.   Kloner RA. No-reflow phenomenon: maintaining vascular integrity. J Cardiovasc Pharmacol Ther. United

641   States; 2011;16: 244–250. doi:10.1177/1074248411405990

642   17.   Granger DN, Kvietys PR. Reperfusion therapy—What's with the obstructed, leaky and broken

643   capillaries? Pathophysiology. Elsevier B.V.; 2017. pp. 213–228. doi:10.1016/j.pathophys.2017.09.003

644   18.   O'Farrell FM, Attwell D. A role for pericytes in coronary no-reflow. Nature Reviews Cardiology. Nature

645   Publishing Group; 2014. pp. 427–432. doi:10.1038/nrcardio.2014.58

646   19.   Yemisci M, Gursoy-Ozdemir Y, Vural A, Can A, Topalkara K, Dalkara T. Pericyte contraction induced
647   by oxidative-nitrative stress impairs capillary reflow despite successful opening of an occluded cerebral
648   artery. Nat Med. Nature Publishing Group; 2009;15: 1031–1037. doi:10.1038/nm.2022

649   20.   Chueh J-Y, Puri AS, Wakhloo AK, Gounis MJ. Risk of distal embolization with stent retriever
650   thrombectomy and ADAPT. J Neurointerv Surg. England; 2016;8: 197–202. doi:10.1136/neurintsurg-
651   2014-011491

652   21.   Bonati LH, Jongen LM, Haller S, Flach HZ, Dobson J, Nederkoorn PJ, et al. New ischaemic brain lesions
653   on MRI after stenting or endarterectomy for symptomatic carotid stenosis: a substudy of the International
654   Carotid Stenting Study (ICSS). Lancet Neurol. England; 2010;9: 353–362. doi:10.1016/S1474-
655   4422(10)70057-0

656   22.   Konduri PR, Marquering HA, van Bavel EE, Hoekstra A, Majoie CBLM. In-Silico Trials for Treatment
657   of Acute Ischemic Stroke. Front Neurol. Frontiers Media S.A.; 2020;11: 558125.
658   doi:10.3389/fneur.2020.558125

659   23.   van Veluw SJ, Shih AY, Smith EE, Chen C, Schneider JA, Wardlaw JM, et al. Detection, risk factors,
660   and functional consequences of cerebral microinfarcts. Lancet Neurol. 2017;16: 730–740.
661   doi:10.1016/S1474-4422(17)30196-5

662   24.   Chueh J-Y, Kühn AL, Puri AS, Wilson SD, Wakhloo AK, Gounis MJ. Reduction in Distal Emboli With
663   Proximal Flow Control During Mechanical Thrombectomy. Stroke. 2013;44: 1396–1401.
664   doi:10.1161/STROKEAHA.111.670463

665   25.   Nishimura N, Schaffer CB, Friedman B, Lyden PD, Kleinfeld D. Penetrating arterioles are a bottleneck
666   in the perfusion of neocortex. Proc Natl Acad Sci U S A. National Academy of Sciences; 2007;104: 365–
667   370. doi:10.1073/pnas.0609551104

668   26.   Schaffer CB, Friedman B, Nishimura N, Schroeder LF, Tsai PS, Ebner FF, et al. Two-Photon Imaging of
669   Cortical Surface Microvessels Reveals a Robust Redistribution in Blood Flow after Vascular Occlusion.
670   PLOS Biol. Public Library of Science; 2006;4: e22. Available:
671   https://doi.org/10.1371/journal.pbio.0040022

672   27.   Shih AY, Blinder P, Tsai PS, Friedman B, Stanley G, Lyden PD, et al. The smallest stroke: Occlusion of
673   one penetrating vessel leads to infarction and a cognitive deficit. Nat Neurosci. Nat Neurosci; 2013;16:
674   55–63. doi:10.1038/nn.3278

675   28.   Van Der Wijk AE, Lachkar N, De Vos J, Grootemaat AE, Van Der Wel NN, Hordijk PL, et al.
676   Extravasation of Microspheres in a Rat Model of Silent Brain Infarcts. Stroke. Lippincott Williams and
677   Wilkins; 2019;50: 1590–1594. doi:10.1161/STROKEAHA.119.024975

678   29.   Schmid F, Conti G, Jenny P, Weber B. The severity of microstrokes depends on local vascular topology
679   and baseline perfusion. bioRxiv. 2020; 2020.07.05.188565. doi:10.1101/2020.07.05.188565

680   30.   Hodneland E, Hanson E, Sævareid O, Nævdal G, Lundervold A, Šoltészová V, et al. A new framework
681   for assessing subject-specific whole brain circulation and perfusion using mri-based measurements and a
682   multiscale continuous flow model. PLoS Comput Biol. Public Library of Science; 2019;15: e1007073.
683   doi:10.1371/journal.pcbi.1007073

684   31.   Jozsa TI, Padmos RM, Samuels N, El-Bouri WK, Hoekstra AG, Payne SJ. A porous circulation model of
685   the human brain for in silico clinical trials in ischaemic stroke. Interface Focus. 2020;In Press.

686   32.   El-Bouri WK, Payne SJ. Multi-scale homogenization of blood flow in 3-dimensional human cerebral
687   microvascular networks. J Theor Biol. 2015;380: 40–47. doi:http://dx.doi.org/10.1016/j.jtbi.2015.05.011

688   33.   El-Bouri WK, Payne SJ. Investigating the effects of a penetrating vessel occlusion with a multi-scale
689   microvasculature model of the human cerebral cortex. Neuroimage. Academic Press; 2018;172: 94–106.
690   doi:10.1016/J.NEUROIMAGE.2018.01.049

691   34.   Park CS, Payne SJ. A generalized mathematical framework for estimating the residue function for
692   arbitrary vascular networks. Interface Focus. Royal Society; 2013;3: 20120078.
693   doi:10.1098/rsfs.2012.0078

694   35.   Linninger AA, Gould IG, Marinnan T, Hsu CY, Chojecki M, Alaraj A. Cerebral Microcirculation and
695   Oxygen Tension in the Human Secondary Cortex. Ann Biomed Eng. Springer US; 2013;41: 2264–2284.
696   doi:10.1007/s10439-013-0828-0

697   36.   Lorthois S, Cassot F, Lauwers F. Simulation study of brain blood flow regulation by intra-cortical

698   arterioles in an anatomically accurate large human vascular network. Part II: flow variations induced by

699   global or localized modifications of arteriolar diameters. Neuroimage. United States; 2011;54: 2840–

700   2853. doi:10.1016/j.neuroimage.2010.10.040

701   37.   Schmid F, Tsai PS, Kleinfeld D, Jenny P, Weber B. Depth-dependent flow and pressure characteristics in

702   cortical microvascular networks. PLOS Comput Biol. Public Library of Science; 2017;13: e1005392.

703   doi:10.1371/journal.pcbi.1005392

704   38.   Gkontra P, El-Bouri WK, Norton K, Santos A, Popel AS, Payne SJ, et al. Dynamic Changes in

705   Microvascular Flow Conductivity and Perfusion After Myocardial Infarction Shown by Image-Based

706   Modeling. J Am Heart Assoc. 2019;8. doi:10.1161/JAHA.118.011058

707   39.   El-Bouri WK, Payne SJ. A statistical model of the penetrating arterioles and venules in the human cerebral

708   cortex. Microcirculation. 2016;23: 580–590. doi:10.1111/micc.12318

709   40.   Cassot F, Lauwers F, Fouard C, Prohaska S, Lauwers-Cances V. A novel three-dimensional computer-

710   assisted method for a quantitative study of microvascular networks of the human cerebral cortex.

711   Microcirculation. 2006/01/06. 2006;13: 1–18. doi:10.1080/10739680500383407

712   41.   Cassot F, Lauwers F, Lorthois S, Puwanarajah P, Cances-Lauwers V, Duvernoy H. Branching patterns

713   for arterioles and venules of the human cerebral cortex. Brain Res. 2009/12/17. 2010;1313: 62–78.

714   doi:10.1016/j.brainres.2009.12.007

715   42.   Lauwers F, Cassot F, Lauwers-Cances V, Puwanarajah P, Duvernoy H. Morphometry of the human

716   cerebral cortex microcirculation: general characteristics and space-related profiles. Neuroimage.

717   2007/11/13. 2008;39: 936–948. doi:10.1016/j.neuroimage.2007.09.024

718   43.   Cassot F, Lauwers F, Lorthois S, Puwanarajah P, Duvernoy H. Scaling laws for branching vessels of

719   human cerebral cortex. Microcirculation. 2009/03/21. 2009;16: 331–44, 2 p following 344.

720   doi:10.1080/10739680802662607

721   44.   Chueh JY, Wakhloo AK, Gounis MJ. Neurovascular modeling: small-batch manufacturing of silicone

722   vascular replicas. AJNR Am J Neuroradiol. 2009;30: 1159–1164. doi:10.3174/ajnr.A1543

723   45.   Chueh JY, Wakhloo AK, Hendricks GH, Silva CF, Weaver JP, Gounis MJ. Mechanical Characterization

724   of Thromboemboli in Acute Ischemic Stroke and Laboratory Embolus Analogs. Am J Neuroradiol.

725   2011;32: 1237 LP – 1244. doi:10.3174/ajnr.A2485

726 46. Pries AR, Secomb TW. Microvascular blood viscosity in vivo and the endothelial surface layer. Am J

727   Physiol Circ Physiol. 2005;289: H2657–H2664. doi:10.1152/ajpheart.00297.2005

728 47. Su SW, Catherall M, Payne S. The influence of network structure on the transport of blood in the human

729   cerebral microvasculature. Microcirculation. 2011/11/25. 2012;19: 175–187. doi:10.1111/j.1549-

730   8719.2011.00148.x

731 48. Shipley RJ, Chapman SJ. Multiscale Modelling of Fluid and Drug Transport in Vascular Tumours. Bull

732   Math Biol. Springer-Verlag; 2010;72: 1464–1491. doi:10.1007/s11538-010-9504-9

733 49. Peyrounette M, Davit Y, Quintard M, Lorthois S. Multiscale modelling of blood flow in cerebral

734   microcirculation: Details at capillary scale control accuracy at the level of the cortex. PLoS One. Public

735   Library of Science; 2018;13: e0189474. Available: https://doi.org/10.1371/journal.pone.0189474

736 50. Rohan E, Lukeš V, Jonášová A. Modeling of the contrast-enhanced perfusion test in liver based on the

737   multi-compartment flow in porous media. J Math Biol. 2018;77: 421–454. doi:10.1007/s00285-018-1209-

738   y

739 51. Risser L, Plouraboue F, Cloetens P, Fonta C. A 3D-investigation shows that angiogenesis in primate

740   cerebral cortex mainly occurs at capillary level. Int J Dev Neurosci. 2008/11/29. 2009;27: 185–196.

741   doi:10.1016/j.ijdevneu.2008.10.006

742 52. Tamaki K, Heistad DD. Response of cerebral arteries to sympathetic stimulation during acute

743   hypertension. Hypertension. 1986/10/01. 1986;8: 911–917.

744 53. Logg A, Mardal KA, Wells GN. Automated solution of differential equations by the finite element

745   method. Lect Notes Comput Sci Eng. 2012;84 LNCSE: 1–736. doi:10.1007/978-3-642-23099-8_1

746 54. Schmid F, Barrett MJP, Jenny P, Weber B. Vascular density and distribution in neocortex. Neuroimage.

747   2017; doi:http://dx.doi.org/10.1016/j.neuroimage.2017.06.046

748 55. Duvernoy HM, Delon S, Vannson JL. Cortical blood vessels of the human brain. Brain Res Bull. Elsevier;

749   1981;7: 519–579. doi:10.1016/0361-9230(81)90007-1

750   56.   Hyde ER, Michler C, Lee J, Cookson AN, Chabiniok R, Nordsletten D a, et al. Parameterisation of multi-

751   scale continuum perfusion models from discrete vascular networks. Med Biol Eng Comput. 2013;51: 557–

752   70. doi:10.1007/s11517-012-1025-2

753   57.   Herdin M, Czink N, Özcelik H, Bonek E. Correlation matrix distance, a meaningful measure for

754   evaluation of non-stationary MIMO channels. IEEE Vehicular Technology Conference. 2005. pp. 136–

755   140. doi:10.1109/vetecs.2005.1543265

756

8   Supporting Information

S1 Table. The main statistics for the distribution of permeabilities in each layer of the healthy voxels (for 100 voxels). The first 4 layers can be approximated as log-normal. The p-value is the Mann-Whitney U-test between adjacent layers to determine if adjacent layers have similar distributions of permeability. For comparison, the capillary bed permeability is 4.28×10^{-4} mm^3 s kg^{-1}

S2 Table. The main statistics for the distribution of coupling coefficients in each layer of the healthy voxels (for 100 voxels). The first 4 layers can be approximated as log-normal. The p-value is the Mann-Whitney U-test between adjacent layers to determine if adjacent layers have similar distributions of coupling coefficients.

S1 Fig. a) A scatter plot of the coupling coefficients of the 100 voxels at each of the 6 depth layers. The mean arteriolar coupling coefficient is indicated with a red star at each layer. b) A quadratic line of best fit over the median coupling coefficients at each layer – error bars are interquartile ranges

S2 Fig. a-f) The drop in permeability with respect to volume fraction blocked over the 6 layers, starting with the top layer a) and ending at the bottom layer f).

772   **S3 Fig. a-f) The change in coupling coefficients with respect to volume fraction blocked over the**

773   **6 layers, starting with the top layer a) and ending at the bottom layer f)**

774   **S4 Fig. Permeability drops for 3 different sampled clot distributions over 100 voxel geometries.**

775   **Results are shown for the middle layer in the voxels.**

776   **S5 Fig. A comparison of the coupling coefficient drop against volume fraction occluded for 3**

777   **different voxel geometries simulated with 100 different clot distributions (for the ADAPT**

778   **technique, hard clot) a) Voxel 1, b) Voxel 4, c) Voxel 31**

779   **S6 Fig. A comparison of the effect of hard and soft clots on permeability drops with respect to**

780   **volume fraction occluded a) Hard clot for all 100 voxels b) Soft clot for all 100 voxels, c) Hard**

781   **clot for Voxel 1 simulated with 100 clot distributions, d) Soft clot for Voxel 1 simulated with 100**

782   **clot distributions, e) Hard clot for Voxel 4 simulated with 100 clot distributions, f) Soft clot for**

783   **voxel 4 simulated with 100 clot distributions**